MNE 32 (2026) 100373

Contents lists available at ScienceDirect

Micro and Nano Engineering

journal homepage: www.sciencedirect.com/journal/micro-and-nano-engineering

Research paper

Monitoring vibrational fingerprints of polypeptide monolayers by plasmonic nanoantennas-enhanced infrared absorption☆

Santos Merino [a,b,*], Alberto Villar [a], Ruth Díez-Ahedo [a], Gabriel Ortega [c,d], Anna Kimmel [e], Federico Marchesin [e,f], Irina V. Lebedeva [e,f], Albert Guerrero [g], Jorge Espina [h], Mario Zapata-Herrera [i,j], Javier Aizpurua [b,d,j], Mónica García-Mota [e]

[a] Surface Chemistry and Nanotechnologies Unit, Tekniker, Eibar 20600, Spain
[b] Departamento de Electricidad y Electrónica, Universidad del País Vasco UPV/EHU, 48940 Leioa, Spain
[c] CIC bioGUNE, Basque Research and Technology Alliance (BRTA), Bizkaia Science and Technology Park, Building 800, 48160 Derio, Spain
[d] Ikerbasque, Basque Foundation for Science, 48009, Bilbao, Bizkaia, Spain
[e] Simune Atomistics, Tolosa Hiribidea 76, 20018 Donostia-San Sebastián, Spain
[f] CIC nanoGUNE BRTA, Tolosa Hiribidea 76, 20018 Donostia-San Sebastián, Spain
[g] Instituto de Microelectrónica de Barcelona (IMB-CNM, CSIC), Bellaterra, Barcelona, Spain
[h] Servicios Científico-Técnicos, Universidad de Oviedo, Fernando Bongera s/n, 33006 Oviedo, Spain
[i] Materials Physics Center (CSIC-UPV/EHU), Manuel de Lardizabal 5, 20018, Donostia-San Sebastián, Guipuzkoa, Spain
[j] Donostia International Physics Center (DIPC), Paseo Manuel de Lardizabal 4, 20018, Donostia-San Sebastián, Gipuzkoa, Spain

ARTICLE INFO

Keywords:
Plasmonic nanoantennas
Density functional theory (DFT)
Surface-enhanced infrared absorption (SEIRA)
TRP-cage protein

ABSTRACT

Proteins and peptides play a central role in the biochemical processes of living cells. In such complex environments, their functionality depends not only on their molecular composition but also on their three-dimensional structure. Infrared vibrational spectroscopy is a powerful technique for studying protein conformations, but its inherent low sensitivity limits its applicability. This limitation can be overcome by Surface-Enhanced Infrared Absorption (SEIRA) spectroscopy, which amplifies molecular vibrational modes through coupling with the resonances of periodic plasmonic nanoantenna arrays. However, the SEIRA response depends on the orientation of the target molecule relative to the near-field distribution induced at the nanostructures, hindering the extraction of quantitative information and the identification of different vibrational modes. In this study, firstly the vibrational fingerprint of the TRP-cage miniprotein is studied by performing density functional theory (DFT) calculations of its amide I and amide II vibrational modes. In parallel, a biofunctionalization protocol was established to bind the protein to the gold surface of the nanoantennas with a controlled orientation, minimizing steric hindrance and allowing the peptide to oscillate at its natural frequencies. The design and fabrication of gold plasmonic nanoresonators (Au nanoantennas) enable the detection of characteristic vibrational features of the TRP-cage, revealing both low- and high-frequency components of the amide I band, as well as contributions from the amide II region. Extending this strategy to other proteins could enable the investigation of different conformational variants in response to external stimuli such as pH, temperature, or chemical environment, ultimately contributing to the development of a comprehensive theoretical and experimental IR absorption database for the identification of vibrational modes within the amide I and II bands of proteins.

1. Introduction

Enhanced vibrational spectroscopy is a technique based on a transduction mechanism for molecular sensing that offers high specificity and sensitivity for molecular detection. It works by collecting the vibrational fingerprints of target molecules through the analysis of signals generated by infrared (IR) absorption and/or Raman scattering [1]. These signals can be significantly amplified by the generation of strong local electromagnetic fields at specific frequencies where IR radiation is absorbed or visible Raman excitation laser light is efficiently coupled with the

☆ This article is part of a Special issue entitled: 'Microsystems 2025' published in Micro and Nano Engineering.

* Corresponding author at: Surface Chemistry and Nanotechnologies Unit, Tekniker, Eibar 20600, Spain.
E-mail address: santos.merino@tekniker.es (S. Merino).

https://doi.org/10.1016/j.mne.2026.100373
Received 6 March 2026; Received in revised form 4 June 2026; Accepted 20 June 2026
Available online 22 June 2026

vibrations. These high local electromagnetic fields can be obtained using metasurfaces, formed by 2D arrays of subwavelength artificial structures, which provide a versatile platform for tailoring light-matter interactions in the visible and infrared spectral ranges [2–4]. When composed of metallic (plasmonic) building blocks such as gold nanoantennas or alternatively, of low-loss dielectric and hybrid nanocavities, they enable precise spectral alignment between localized electromagnetic modes in the IR and molecular vibrational modes, enabling effective Surface-Enhanced Infrared Absorption (SEIRA) [5]. A similar design in the visible range of the spectrum (typically with smaller structures) enables Surface-Enhanced Raman Scattering (SERS). By tuning the geometry and dielectric environment of these building blocks, metasurfaces can produce intense near-fields that amplify the signal from molecular vibrational fingerprints, enabling ultrasensitive biosensing and molecular detection. Alternatively, arrays of plasmonic nanoresonators can also be used in this context, with the optical response arising from the sum of individual localized surface plasmon resonances (LSPRs) rather than from collective effects [6]. The spectroscopic signals detected by both SEIRA and SERS strongly depend on how the target molecules are oriented on the metasurfaces, as this determines how the molecules align with the local electromagnetic fields, and thus which chemical bonds signals are enhanced.

Particularly, for SEIRA analysis, certain vibrational modes may couple strongly when their dipole moments align with the local field along the antenna surface, while others couple only weakly or not at all [7]. Therefore, the way the molecule is adsorbed (its tilt angle, binding group, and location relative to the nanoantenna hot spots) strongly affects which vibrational bands are enhanced. Typically, surface deposition relies on physicochemical adsorption. However, this approach produces multiple random orientations (see schematics in Fig. 1), resulting in molecules coupling with different efficiencies to the antenna's local field. Consequently, identifying a molecule based on its vibrational fingerprints (both its vibrational frequencies and corresponding cross sections) is much more complex, since the same molecule can exhibit very different intensities depending on how it binds to the antenna surface [8].

Aiming to achieve a more homogeneous deposition, other surface functionalization strategies rely on more specific chemical reactions. For example, deposition via amide bond between an amine-incorporating ligand and a carboxylic-functionalized surface has been used to study conformational changes of poly-lysine peptides with a gold nanoantenna coated with a lipid monolayer, formed by a mixture of two lipids (a hydroxyl-terminated lipid for monolayer structure and a carboxyl-terminated lipid for surface functionalization). This approach provides a well-defined chemistry, and a rational way of controlling the distance to the surface as well as between neighboring molecules [9]. However, biomolecules, and more particularly proteins, very often present multiple amine and carboxylic groups, thus resulting in protein binding to the surface at multiple sites and conformations. Other approaches leverage the higher specificity of protein–ligand interactions. For example, interaction of streptavidin with biotinylated gold plasmonic resonators were used to study streptavidin binding and quantify its concentration in solution [10]. Nevertheless, this strategy does not ensure a unique orientation because streptavidin has four biotin-binding sites located on different faces of the protein, allowing it to bind in multiple spatial configurations. Therefore, the protein adopts heterogeneous orientations on the surface, leading to a correspondingly heterogeneous SEIRA signal. Other strategies combine protein engineering and biocompatible chemistry to achieve a specific and well-defined protein deposition on surfaces [11]. In particular, cysteine–maleimide chemistry has enabled site-specific immobilization of the protein α-synuclein by introducing a cysteine residue at its C-terminus, using the free thiol for deposition onto a maleimide-coated gold surface. This enabled analyzing the plasmonically enhanced amide I signatures to detect synuclein conformational changes, associated with protein aggregation in neurodegenerative diseases [12]. However, this study remains at an empirical level, missing a more fundamental understanding of the interplay between surface vibrational frequencies and protein–surface interactions. To sum up, despite extensive work on detecting various molecules using SEIRA spectroscopy, most studies have relied on physical adsorption or chemically favored orientations, leading to non-uniform SEIRA signals that vary significantly depending on how the target molecules are oriented on the surface, complicating both empirical and theoretical analysis.

In this work, arrays of gold nanoresonators were manufactured and resonant SEIRA was employed to detect the vibrational fingerprints of tryptophan cage (TRP-cage) protein. This artificial miniprotein is one of the smallest proteins known to adopt a stable, cooperative, and compact fold [13,14]. Due to its small size and fold simplicity, it has been extensively used in fundamental studies in protein folding and stability,

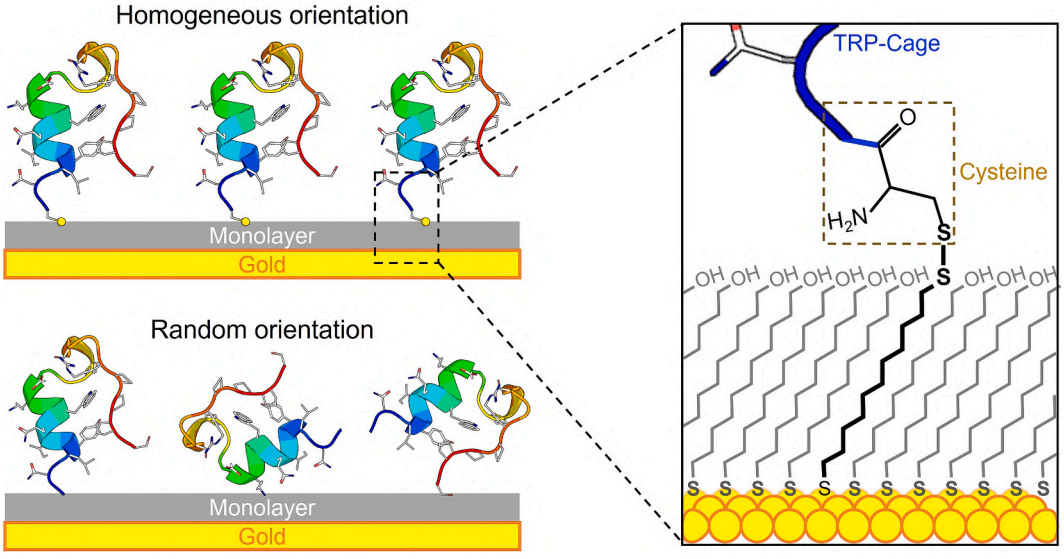

Fig. 1. The figure illustrates the importance of achieving a uniform orientation of the TRP-cage protein on the surface (top left cartoon) to obtain a consistent SEIRA signal, as opposed to random orientations (bottom left cartoon). It also highlights the relevance of maintaining a defined spacing between molecules to allow for unrestricted peptide vibrations. The inset shows a detailed view of the TRP-cage peptide immobilized onto a mixed self-assembled monolayer of thiols (1,11-undecanethiol in black, and 11-mercapto-1-undecanol in gray) via a cysteine residue located at its terminal position.

as well as in theoretical and computational studies. Ab initio calculations are performed within the framework of density functional theory (DFT) to investigate the vibrational fingerprints of the protein surrounded by gold plasmonic surfaces. These vibrational fingerprints guided the design of the gold nanoresonators capable of generating strong local electromagnetic fields precisely at the wavelength of the amide I vibrational band of the TRP-cage. To enhance the protein's vibrational signal, the TRP-cage is positioned within the local electric field generated in the close proximity of the nanoantennas at their plasmonic resonances. Appropriate lateral spacing was achieved using a mixed self-assembled monolayer of thiols (one species enabling protein binding and another preventing non-specific adsorption) thus allowing the molecules to vibrate at their natural frequencies. Furthermore, to ensure a uniform binding orientation and to avoid multiple attachment modes on the gold surface, a cysteine residue was introduced at the terminal position of the TRP-cage (Fig. 1). The SEIRA signal is studied using this configuration and the amide I and amide II vibrational bands of the TRP are detected and analyzed. The results reveal that the different vibrational modes exhibit a semi-discrete behavior rather than a continuous profile, showing good agreement with theoretical predictions from DFT and electrodynamic simulations.

This work combines a theoretical study of the amide I and amide II vibrational bands of a peptide with a uniform peptide orientation on the surface revealing a semi-discrete behavior of the amide I band.

2. Materials and methods

2.1. Materials and reagents

The TRP-cage protein sequence C-NLYIQWLKDGGPSSGRPPPS with a purity of 95% was purchased from Merck Life Science (United Kingdom). The peptide was synthesized with a cysteine residue added at the N-terminal position of the protein and supplied in lyophilized form. Deuterium oxide with 99.95% of purity was purchased from ThermoFisher Scientific and supplied in Acroseal packaging to minimize solvent moisture uptake. Phosphate Buffer Saline (PBS), 1,11-undecanedithiol and 11-mercapto-1-undecanol were purchased from Sigma-Aldrich (Spain). 2-(N-morpholino)ethanesulfonic acid (MES), tris(2-carboxyethyl)phosphine (TCEP), and NaCl were purchased from Scharlab (Spain).

Calcium Fluoride (CaF_2) wafers were purchased from Redoxme AB (Sweden). For the microfluidic cell fabrication, the following materials were used: a pressure-sensitive adhesive thin film (ARsealTM 90,880, Adhesive research), polycarbonate Lexan 8010 MC (Konig), Stand-alone female mini luer and male mini luer plug (ChipShop), and double side adhesive tape 3 M™ 9088–200.

2.2. Ab initio calculations of vibrational spectra

2.2.1. Atomistic model

The TRP-cage protein was modeled using the structure 1L2Y, which was obtained by nuclear magnetic resonance (NMR) and retrieved from the RCSB database [13] (Fig. S1). To describe the influence of the surface of the nanoantenna on the molecular binding, a 55-atom gold cluster (Au_{55}) was chosen as a model system because it provides a reasonable balance between computational feasibility and an accurate representation of the local electronic and structural properties of extended gold surfaces. This cluster size is large enough to capture key surface effects, such as charge redistribution and molecule–metal interactions, while remaining small enough to be efficiently treated in DFT calculations. In the simulations, the TRP-cage protein was anchored to this gold cluster via its cysteine residue, utilizing 1,11-undecanedithiol as the connector molecule (Fig. S2).

2.2.2. Methodology for ab initio calculations

The calculations were performed using the Atomistic Simulation Advanced Platform (ASAP) package [15,16], which provides comprehensive tools for structure visualization, input file preparation, remote job execution, and result analysis. The platform employs automatic workflows for geometry optimization and vibrational spectrum calculations that rely on the Atomic Simulation Environment (ASE) [17].

The DFT computational engine was a preview version [18] of SIESTA [19,20] featuring a recently implemented implicit solvent method [21] using the BigDFT PSolver library [22]. The electronic structure calculations were carried out using an optimized double-zeta polarized (DZP) basis set and the PSF pseudopotentials integrated in ASAP with a real-space mesh cutoff of 100 Ry. The Perdew-Burke-Ernzerhof (PBE) [23] exchange-correlation functional was used for tests on the isolated TRP-cage, while the vdW-DF functional [24,25] was selected for the TRP-cage anchored to the metal cluster to accurately include dispersion interactions. The water environment was simulated using the soft-sphere implicit solvent model [21] with a dielectric constant of 78.36 [22] and sphere transition region width of 8 Bohr. To prevent spurious long-range interactions between periodic images, a minimum vacuum or solvent gap of 16 Å was included around all simulated structures. Geometry optimization of both isolated and anchored TRP cages was performed until the residual force was less than 0.02 eV/Å.

2.2.3. Computational vibrational analysis

The vibrational modes of the TRP-cage protein were computed in the harmonic approximation considering atomic displacements of 0.01 Å in all directions and extracting the Hessian matrix using finite differences. To address the significant computational cost associated with the large metal-anchored TRP-cage structure (415 atoms), and to isolate the amide I modes of interest, a simplification was adopted: the coordinates of atoms beyond the amide, amine, and carboxyl groups, as well as the majority of hydrogen atoms, were fixed. Control calculations for the TRP-cage in vacuum confirmed that this constraint introduced a minimal red shift (< 6 cm $^{-1}$) to the amide I modes, a value significantly smaller than the observed frequency shifts induced by the solvent or the gold substrate. Since this shift is significantly smaller than the observed effects caused by the solvent or the gold substrate (as described later in Figs. 2 and 3), the use of this simplification is justified.

2.3. Numerical electromagnetic simulation

To investigate the optical response of the nanoantennas responsible for the SEIRA effect, Maxwell's equations were solved using the Finite Element Method (FEM), as implemented in COMSOL Multiphysics [26]. A lumped port formulation was employed, and periodic (Floquet) boundary conditions were imposed along the in-plane directions of a rectangular unit cell, while scattering boundary conditions were applied along the out-of-plane (z) direction, as described elsewhere [8] (see also Section 3 of the SI). To represent a realistic experimental scenario, a single Au nanorod was placed on top of a CaF_2 substrate (assuming a refractive index $n = 1.4$) within a periodic unit cell, with the antenna positioned at the center of an extended (~50 μm) z-directed computational domain. Accordingly, the physical domains were arranged in a regular rectangular array with a chosen lattice parameter (See Section S3 of the SI for geometrical details). Finally, perfectly matched layers (PMLs) with thickness TPML =5 μm were placed at the top and bottom of the simulation domain, in addition to the scattering boundary conditions along the z-axis to prevent spurious reflections from the interfaces along this direction. All domains in the simulation box were meshed using tetrahedral elements ensuring a maximum element size below $\lambda/10$ to guarantee numerical convergence where λ is the wavelength of the incident light. The element size within the nanorod and its surrounding shell was chosen to be at least one order of magnitude smaller than the characteristic dimensions of the nanoantenna. Mesh convergence was verified by progressively refining the tetrahedral discretization until no significant variations were observed in the calculated reflectance spectra. A similar numerical electromagnetic

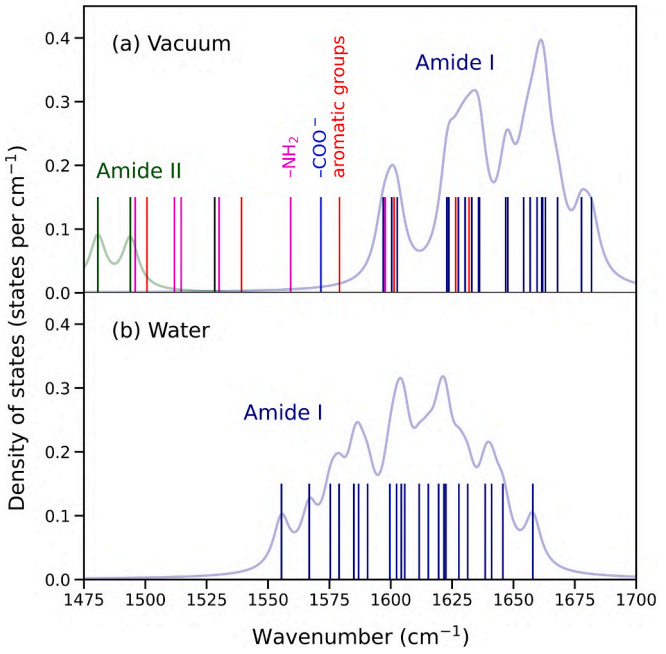

Fig. 2. Calculated vibrational density of states (in states per cm^{-1}) as a function of wavenumber (in cm^{-1}) for an isolated TRP molecule in (a) vacuum and (b) water. The bars indicate the discrete frequencies corresponding to the following vibrational modes: (dark blue) amide I, (dark green) amide II, (red) C═C bond stretching in aromatic rings, (magenta) N—H scissoring in primary $–NH_2$ amine groups, (blue) asymmetric stretching in the $–COO^-$ carboxylate group, and (black) asymmetric stretching in the $–NC(NH_2)_3$ guanidino group. The continuous curves (solid lines) represent the final spectra for the amide I (blue) and amide II (green) bands. These curves are generated solely from their respective amide I and amide II discrete modes by applying a Lorentzian broadening function with a full width at half maximum of 8 cm^{-1}. The height of the bars is scaled by a factor of 0.15 for clarity. (For interpretation of the references to colour in this figure legend, the reader is referred to the web version of this article.)

simulation procedure implemented in Section 1 of the SI of reference [8] was adopted.

2.4. Micro and nanofabrication

Arrays of Au nanorod antennas with varying lengths were fabricated using electron beam lithography (EBL) followed by gold *lift-off*. 1 × 1 mm arrays were fabricated each of them with different antenna lengths. The arrays were patterned on top of a CaF_2 wafer using EBL on a MMA-PMMA double layer (200 nm thickness) and a conductive resist layer to dissipate charge. Later, a Ti and Au evaporation (5 nm + 60 nm) followed by a metal *lift-off* process were carried out. In this process, some alignment marks were also included, close to the patterns enabling the alignment of the nanoantennas and their location within the sample using the microscope. The methodology used to transfer the aforementioned patterns to the CaF_2 substrate is the described as follows. The substrates were first cleaned in acetone and isopropanol using ultrasonic bath, after that, a dehydration step at 180 °C was performed on a hot-plate to enhance the resist adhesion and deposition. Once the samples were prepared, the resist layers were deposited onto the substrates. First, a layer of MMA EL6 was spin-coated at 1500 rpm for 60 s and soft-baked on a hot plate at 180 °C for 1 min. Next, a layer of PMMA 950 k A2 was also spin-coated at 1500 rpm for 60 s and soft-baked on a hot plate at 180 °C for 1 min. Finally, a conductive layer of Electra92 was spin-coated at 2000 rpm for 60 s and soft-baked on a hot plate at 90 °C for 2 min. The patterns were then transferred by EBL (Raith-150TWO, Germany). Following electron-beam exposure, the conductive layer was removed by immersing the sample in DI H_2O at room temperature for 60 s. The sample was then developed in a MIBK:IPA mixture (1:3) for 30 s and rinsed in IPA for 30s. Once the samples were ready, they were brought to an electron beam evaporation system (UNIVEX 450B – Leybold, Germany) where a 5 nm of Ti layer, used to enhance the metal adhesion to the substrate, followed by a 60 nm layer of Au were deposited. Finally, a metal *lift-off* process was carried out using acetone and avoiding the use of ultrasonic bath to preserve the transferred nanorods.

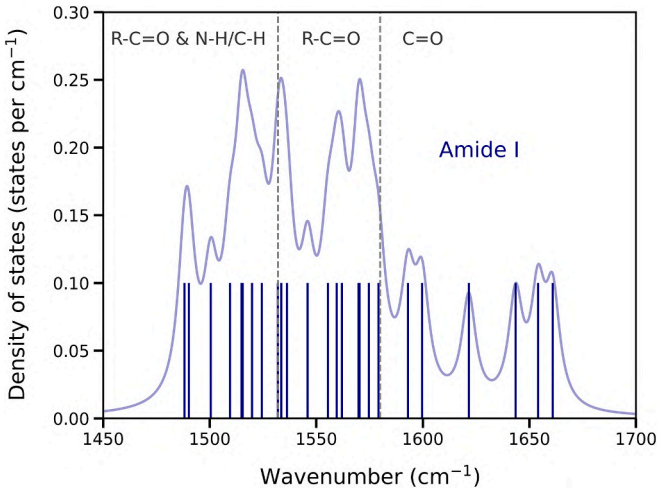

Fig. 3. Calculated vibrational density of states (in states per cm^{-1}) as a function of wavenumber (in cm^{-1}) for the amide I vibrational band of the TRP peptide anchored to a Au_{55} cluster in water. The vertical bars represent the discrete frequencies of the calculated amide I normal modes. The continuous spectrum (solid line) is generated by convolving these discrete modes with a Lorentzian broadening function with a full width at half maximum of 8 cm^{-1} to simulate experimental spectral line shapes. The height of the bars is scaled by a factor of 0.1 for clarity. The vertical dashed lines indicate the spectral regions corresponding predominantly to decoupled C═O stretching, R-C=O stretching, and R-C=O stretching coupled with N-H/C-H bending modes (R-C=O & N-H/C-H).

2.5. Biofunctionalization protocol

An ethanolic mixture of lipids, comprised of 11-mercapto-1-undecanol and 1,11-undecanedithiol in a 9:1 ratio, was used to form a passivating self-assembled monolayer (SAM) on gold. To do this, the gold surface was soaked with the mixture and incubated for 4 h at room temperature.

A 2-(N-morpholino) ethanesulfonic acid (MES) buffer was used to dissolve the peptide to 100 μM concentration. A certain amount of NaCl (20 mM MES, pH 6.5, and 100 mM NaCl) was added to adjust the ionic strength and stabilize the protein's surface charge and keep the native conformation. Subsequently, the thiol group was reduced by incubation with 1 mM tris-(2-carboxyethyl)phosphine (TCEP) for 1 h, and the sample was then diluted in PBS buffer (20 mM sodium phosphate, pH 6.5, containing 100 mM NaCl) to obtain a final peptide concentration of 1 μM, and removing the TCEP by dilution and phosphate-induced precipitation. The gold was then incubated with the peptide mixture for 1 h at room temperature and then gently rinsed with heavy water. The substrate containing the gold nanorods was subsequently enclosed in a microfluidic cell and filled with heavy water for subsequent SEIRA characterization.

For the random adsorption controls, we follow the same biofunctionalization protocol but forming instead a homogeneous monolayer of 11-mercapto-1-undecanol alone.

2.6. Microfluidic cell fabrication

A disposable microfluidic chamber was manufactured for medium-infrared (mid-IR) absorption measurements to ensure complete sample wetting and uniform coverage across the antenna arrays while minimizing liquid evaporation. The chamber was designed to encapsulate the 1 in. CaF_2 substrate containing the arrays of gold nanorods, following the protocol described below. Briefly, an 80 μm thick double-sided pressure sensitive adhesive (PSA) film was pre-cut to match the cell dimensions, with a designated 1.5 cm × 0.5 cm area to define the chamber's boundaries. Finally, to close the chamber a polycarbonate (PC) film containing a precut inlet and outlet was adhered on the top of PSA. Inlet/ outlet connectors can be used to facilitate the sample introduction and extraction and they can be sealed after pipetting the sample with scotch tape or plugs to avoid evaporation or sample loss. One hour after introducing the TRP-cage solution, the assembled cell was inverted and mounted for Fourier-transform infrared spectroscopy (FTIR) measurements in an inverse reflection configuration.

2.7. SEIRA spectroscopy

SEIRA signals were studied by Fourier-transform infrared (FTIR) spectroscopy using a Varian 620-IR FTIR microscope coupled to a Varian 670-IR spectrometer, equipped with a liquid nitrogen-cooled mercury cadmium telluride detector and referenced to a gold mirror. All SEIRA measurements were performed in reflection mode with an Agilent objective (Numerical Aperture = 0.81) with a Field of Vision of 420 × 420 μm illuminating the chips from the backside. The measurements were performed at a resolution of 2.0 cm^{-1}, with at least 128 scans averaged per sample. Polarization of the infrared radiation was controlled by employing a rotatable Pike 723–2101 polarizer, which was aligned along the long axis of the gold nanorods.

2.8. Data analysis

The TRP-cage infrared fingerprints were extracted by normalizing the sample reflectance spectrum (R) to that of the reference (R_0) obtained from the deuterium oxide (D_2O) in the absence of the molecule. The differential absorbance spectrum (ΔA) was calculated by subtracting a polynomial baseline, fitted by least-squares method from the normalized reflectance spectrum [27].

3. Results and discussion

3.1. DFT mode assignment of TRP-cage and plasmonic antenna design

The isolated TRP-cage mini-protein was initially studied in vacuum over the whole frequency range using DFT calculations to obtain its complete vibrational spectrum (Fig. S3). The atomic motions contributing to individual vibrational modes were visualized, allowing for the identification of the C═O stretching motion that constitutes the amide I band. It was found that these amide I modes are distributed across a wide frequency range, from 1596 to 1681 cm^{-1}, due to the presence of multiple C═O bonds in varied chemical environments. A more detailed analysis of this spectral range shows that the frequency of the amide I modes is sensitive to the oxygen atom involvement in hydrogen bonding (Fig. 2a). Higher frequency modes are characteristic of non-hydrogen-bonded C═O groups, whereas the lower frequency modes are associated with C═O groups strongly engaged in intramolecular hydrogen bonding. Moreover, the character of the vibrations varies across the band, with the modes at the band edges identified as decoupled C═O stretches and those spanning the center of the band corresponding to highly coupled vibrations of multiple amide groups.

In addition to the C═O bond stretching, the amide I region contains overlapping vibrational modes of a different nature (Fig. 2a). Specifically, C═C stretching vibrations from aromatic groups yield peaks at 1632, 1626 and 1601 cm^{-1}, which couple strongly with C═O stretching vibrations at similar frequencies. At the lower-frequency edge of the band (1598 cm^{-1}), a peak related to the scissoring and bending vibrations of N—H bonds in a primary amine group ($-NH_2$) is also observed. Both the C═C stretching modes in aromatic groups and amine modes extend below the low-frequency edge of the amide I band, which is separated from the high-frequency edge of the amide II band found at 1493 cm^{-1}. In the following analysis, these non-C═O vibrations were discarded, as they are expected to yield a much weaker signal in the SEIRA measurements.

To evaluate the effect of the solvent, the vibrations of the isolated TRP-cage peptide in water were computed (Fig. 2b). These calculations revealed that vibrational modes corresponding to the amide I band experience a red shift. The shift is non-uniform across the spectrum, ranging from 20 cm^{-1} at the high-frequency edge to 40 cm^{-1} at the low-frequency edge, but the order of the modes in frequency is generally maintained. The amide I band in this case extends from 1556 to 1658 cm^{-1} and begins to overlap with the asymmetric stretching vibrations in the carboxylate group ($–COO^-$) starting at 1600 cm^{-1}.

To incorporate the effects of the metallic surface of the gold nanoantennas, the TRP-cage molecule anchored to a gold cluster was modeled. The resulting amide I band in this complex system exhibits significant broadening and a red-shift, with its lower-frequency edge extending towards a minimum at 1488 cm^{-1} (Fig. 3). Upon anchoring to the gold substrate via linking molecules, the TRP structure undergoes remarkable conformational changes that are accompanied by a reorganization of the hydrogen-bonding network. This reorganization creates a heterogeneous band profile: atomic groups located close to the gold cluster surface become disconnected from the hydrogen-bonding network and consequently show higher frequencies. Conversely, the lower frequency components exhibit increasingly complex atomic motion. Amide I modes below 1580 cm^{-1} are accompanied by noticeable displacement of the atoms surrounding the carbon and oxygen atoms (R-C═O stretching mode). Below 1530 cm^{-1}, the amide I modes involve complex, cooperative atomic motion, including coupling with N—H and C—H bending in the amine, amide, and alkane groups. Additional contributions to the amide I band are observed from C═O stretching in the cysteine residue amide groups (at 1644 and 1654 cm^{-1}) and its carbonyl group (at 1488 cm^{-1}).

To investigate the amide I vibrational fingerprints of the TRP-cage, the design of the nanoantennas is optimized to achieve a strong resonance of the nanoantennas in the region corresponding to the most intense Au_{ss}–TRP-cage signals in water, following the DFT results presented above. Accordingly, the design targets coupling between the plasmonic modes of the nanoantennas and the relevant vibrational frequencies, using three approximate wavenumbers (1615 cm^{-1}, 1540 cm^{-1}, and 1480 cm^{-1}) as representative values to guide the target in the calculations of the nanoantenna response. The nanoantenna geometry was selected to support a longitudinal plasmonic resonance within the amide I spectral window, i. e, ≈1450–1700 cm^{-1}, as guided by FEM simulations (Section 3 of SI). The simulations for the fabricated geometry (a plasmonic nanoantenna with L = 2.1 μm in Fig. 4b and another one with L = 1.8 μm in the Fig. S4d of SI) shows the expected reflectivity modification upon introducing a protein-containing shell, consistent with resonant coupling in the experimental configuration as it is seen in the next section.

3.2. Nanofabrication, functionalization and IR absorption characterization

The results of the IR response of the nanoantennas provide a guide for fabrication of nanoantennas that produce an optimal spectral match with the selected TRP-cage' s amide I vibrational frequencies. Accordingly, different arrays of nanoantennas, with lengths between 1.8 μm and 2.4 μm, were arranged in a lateral thickness of 300 nm, and a height of 60 nm were designed following a rectangular lattice with $W_X = 3$ μm

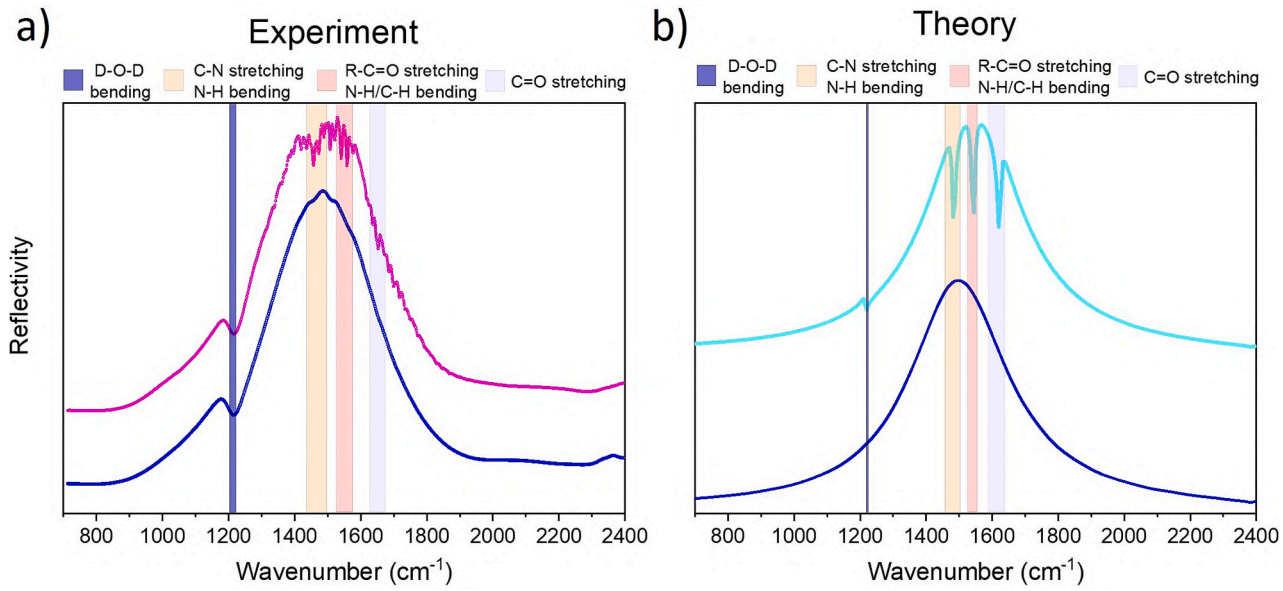

Fig. 4. (a) Reflectance spectra of TRP-cage in 99.95% deuterium oxide (purple line) and reference deuterium oxide (dark blue) measured on arrays of 2.1 μm-long gold nanoantennas. (b) Simulated reflectance spectra of the TRP-cage solution (light blue) and reference deuterium oxide (dark blue) on arrays of 2.1 μm-long gold nanoantennas. The different absorption bands corresponding to TRP-cage and deuterium oxide are indicated by colors, as described in the text in the upper part of the figure. (For interpretation of the references to colour in this figure legend, the reader is referred to the web version of this article.)

and $W_Y = L + 1$ μm. The varying nanoantenna lengths were patterned using EBL followed by gold *lift-off* in separate 1×1 mm^2 arrays, all integrated into a single microfluidic chip. Fig. 5a and b show scanning electron microscopy (SEM) images of the fabricated nanoantennas while Fig. 5c shows a schematic of the encapsulated metasurfaces arrays. Finally, the nanoantennas were functionalized with a mixture of lipids—11-mercapto-1-undecanol and 1,11-undecanedithiol—in a 9:1 ratio, to create both a defined spacing between the peptides (on average, 15 Å) and between them and the gold surface. This configuration allows the peptides to vibrate freely, minimizing steric factors and constraints that could limit their natural motion.

FTIR characterization of encapsulated metasurfaces was done as gold nanoantennas were studied immersed in 99.95% deuterium oxide (D_2O) using the bare nanoantennas as a reference for subsequent TRP-cage samples characterization. D_2O was used instead of H_2O aiming to circumvent the strong absorption of the H-O-H bending mode in the

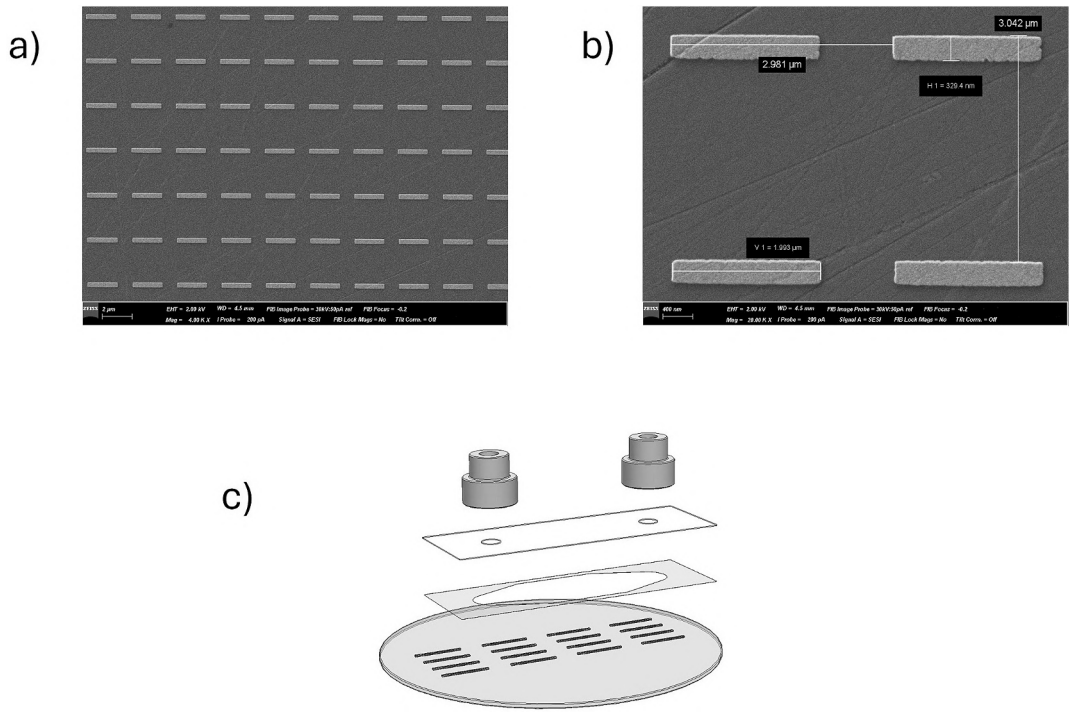

Fig. 5. Images and scheme of fabricated gold nanoantennas and their encapsulation. a) Large field-view scanning electron microscopy (SEM) image, b) high magnification SEM image showing the resonators length (~2 μm), width (~300 nm) and rectangular lattice parameters ($W_x = 3$ μm and $W_Y = L + 1$ μm), c) scheme of the microfluidic cell used to encapsulate gold nanorods on a CaF_2 substrate for sample confinement at certain volume (~25 μL) and posterior infrared absorption measurements. (For interpretation of the references to colour in this figure legend, the reader is referred to the web version of this article.)

spectral region of interest. Fig. 4a shows the reflectance of the samples for both pure D_2O and the TRP-cage sample in D_2O for 2.1 μm (and 1.8 μm in the Fig. S4c) plasmonic nanoantenna length. The FTIR characterization was done with the incident light polarization oriented parallel to the long axis of the plasmonic nanoantennas, as this direction supports the strongest localized electromagnetic field enhancement and therefore maximizes the coupling with molecular vibrational modes. Fig. S5 describes the signal for the 1.8 μm plasmonic nanoantenna length as the incident light is polarized parallel to the long antenna axis and when the polarization is rotated 90° with respect to this axis. The D_2O referenced spectra exhibits broad plasmonic resonances with a Lorentzian-like shape, red shifting by around 150 cm^{-1} as the nanoantenna length increases, in good agreement with the simulations (Fig. 4b and Fig. S4d). A strong absorption feature is observed around 1215 cm^{-1}, which is attributed to the D-O-D bending mode of D_2O [28]. Its relative contribution increases for longer antennas because their plasmonic resonance spectrally approaches this vibrational mode. A weak absorption near 1650 cm^{-1} is also detected and attributed to the H-O-H bending mode of residual H_2O (Fig. S4c). The presence of this small absorption can be justified by the tiny amount of H_2O present in the high-purity D_2O sample and the strong absorption of the H-O-H vibrational mode [8,29]. To validate further the robustness of the FTIR far-field characterization and so the biofunctionalization reproducibility on large areas, the reflectance signal was measured on different sites of each 1 × 1 mm plasmonic nanorods (Fig. S6).

The reflectance signal for TRP-samples shows that plasmonic resonances can be tuned well to the target spectral bands. The coupling of TRP's vibrational modes with antennas plasmonic resonances is clearly observed for the 2.1 μm nanoantenna length. Experimental characterization fits well with the theoretical model (Fig. 4b) in which the molecular permittivity was parameterized using a three-term Lorentz oscillator model, with each Lorentzian resonance assigned to one of the molecule's fundamental vibrational modes represented by the colour bands in Fig. 4a and b. The oscillator strengths, resonance frequencies, and damping constants were adjusted to reproduce the measured SEIRA response. These absorption bands extended from 1450 to 1670 cm^{-1} are attributed to the amide I and amide II's vibrational bands of the peptide, which are associated to the target C═O vibrational modes and the N—C stretching and N—H bending modes of the amide II [30]. It is important to note that the thiol mixture exhibits vibrational bands corresponding to C—H stretching (2900–3100 cm^{-1}), O—H stretching (~3500 cm^{-1}), and S—H stretching (~2500 cm^{-1}) modes, all of which fall well outside the plasmonic resonance range and the characteristic vibrational spectrum of the protein under study.

To compare how the controlled orientational binding of the mini-protein TRP-cage has an influence on the far-field characterization of the analyzed system, the reflectance signal of a randomly adsorbed TRP-cage in heavy water was analyzed. Fig. S7 shows the reflectance signal for two different sites of the 2.1 μm length gold nanorod array. Fig. S7 shows that when the mini-protein is adsorbed randomly on the antenna surface, the vibrational absorptions appear smoother and less intense. This effect arises due to the broader distribution of molecular

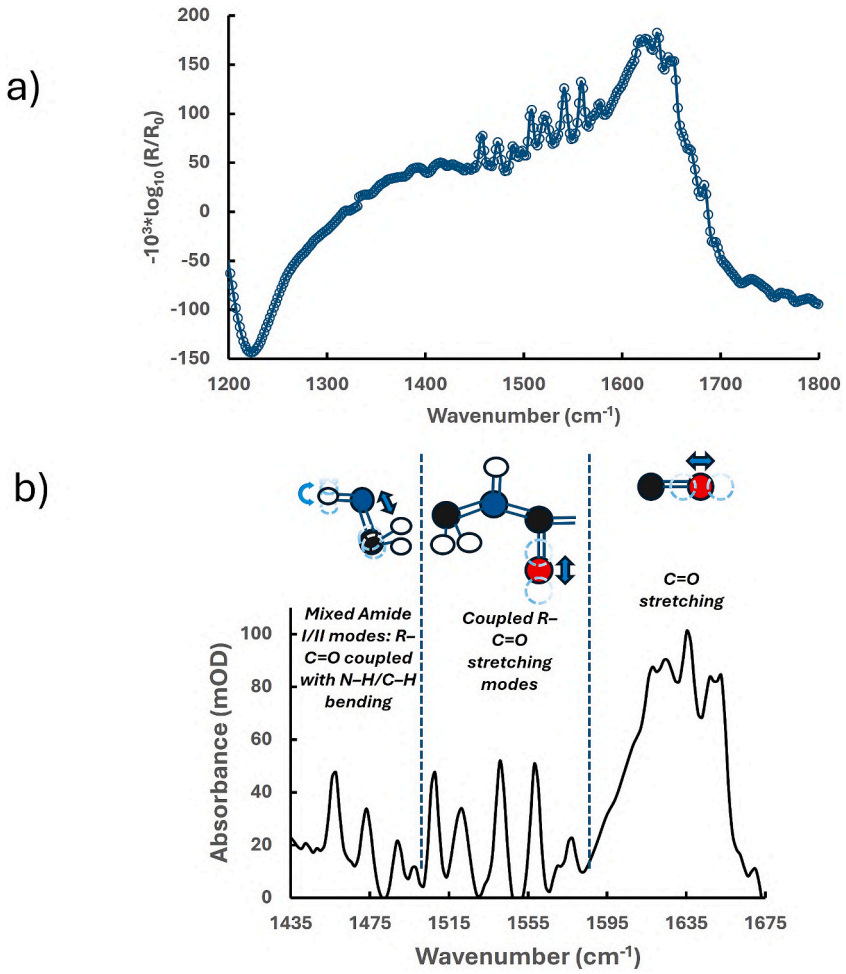

Fig. 6. (a) Normalized reflectance for the 2.1 μm plasmonic nanoantenna length, (b) Baseline-corrected absorbance. Black, red, blue and white represent carbon, oxygen, nitrogen and hydrogen atoms and vibrational modes are envisaged for each spectral range of absorbance. (For interpretation of the references to colour in this figure legend, the reader is referred to the web version of this article.)

orientations generated by random adsorption, each exposing different chemical bonds and alignments to the local plasmonic field, resulting in an averaging effect of the dipole-field coupling. Additionally, Fig. S7 shows that the random adsorption can lead to spatial variations in molecular orientation and local surface coverage, producing signal differences across different regions of the substrate. As a result, both enhancement efficiency and the spectral contrast become less uniform, leading to weaker and more spatially heterogeneous SEIRA responses.

A more detailed analysis of the TRP-cage vibrational fingerprints was obtained by normalizing the reflectance spectrum of the TRP-cage functionalized 2 μm length plasmonic nanoantenna (R) to that of the same metasurface prior to peptide injection (R_0). Thus, the normalized reflectance was calculated as $A = -10^3 * \log_{10}(R/R_0)$ (Fig. 6a) and subsequently corrected (Fig. 6b) by subtracting a polynomial baseline fitted by a least-squares method (Fig. S8).

Following this procedure, the corrected absorbance (Fig. 6b) shows a discrete set of peaks in the target vibrational spectral region. DFT calculations provide information on discrete individual vibrational modes, whereas the experimental absorbance spectrum reflects the broadened collective response arising from the convolution of these modes. Based on the DFT results, these features can be assigned to: (i) C═O stretching (amide I): decoupled C═O stretching modes oriented towards the inner or outer region of the molecule (1580–1650 cm^{-1}), (ii) coupled R–C═O stretching modes: lower frequency R-C═O stretching modes in which the carbonyl group vibration is coupled to extended molecular fragments surrounding the molecule (1500–1580 cm^{-1}) and (iii) Mixed amide I/II modes: R–C═O coupled with N–H/C–H bending: R-C═O stretching modes coupled with N-H/C-H bending modes and C—N stretching and N—H bending modes (1460–1500 cm^{-1}) associated with the amide II band. The correspondence of the low-frequency features to the amide II vibrational band is supported by their reduced intensity compared to amide I [30] as well as by their spectral position below 1500 cm^{-1} [31]. The calculated discrete vibrational modes thus provide a microscopic interpretation of both the spectral broadening and the internal structure of the experimentally observed amide I band.

The observed semi-discrete spectral structure within the amide I region is associated with the intrinsic vibrational response of the TRP-cage molecule, while the plasmonic nanoantennas mainly provide localized electromagnetic enhancement of the molecular vibrational dipoles. In this framework, controlled molecular immobilization reduces orientational averaging effects and improves the coupling between the dominant vibrational dipoles and the longitudinal plasmonic mode of the nanoantennas, allowing a more resolved observation of the vibrational substructure. Because each peptide is anchored through a single cysteine residue and separated from the gold surface and neighboring molecules by the mixed SAM, the orientation of its transition dipole moments with respect to the antenna near field is similar across molecules. As a result, each molecule's dipole moment aligns in the same way with the local electromagnetic field, leading to a higher degree of homogeneity in the spectral response and thus discretization in the vibrational energy levels. In contrast, when molecules bind to the surface without a preferred orientation, the enhanced vibrational signal varies from one molecule to another. This produces an averaged spread of the signal across vibrational modes, resulting in broader absorption features that correspond to the amide I and amide II spectral bands [10]. The fact that the TRP-cage protein is well separated from the gold surface and neighboring molecules allows it to vibrate at its natural frequencies, rather than exhibiting forced vibrations caused by steric constraints from surrounding molecules.

The difference between theoretical calculation for the amide I vibrational band (1490–1660 cm^{-1}) and experimental data (1500–1670 cm^{-1}) is reasonable given the simplified cluster model used in DFT to describe the molecule-metal system. More accurate models including anharmonic effects, larger metallic clusters, explicit solvent, and intermolecular interactions, may influence the SEIRA signal, but modelling these effects by DFT is computationally demanding and out of the scope of this work. The amide II vibrational contribution was not explicitly computed in the current DFT model; however the strong absorptions observed between 1460 and 1500 cm^{-1} are attributed to low frequency R-C═O stretching modes coupled to N—H and C—H bending modes in the amine, amide and alkane groups as well as to the amide II spectral band related to N—C stretching and N—H bending modes. Although higher wavenumbers (1530–1540 cm^{-1}) have been experimentally reported for the amide II vibrational modes of TRP-cage in aqueous solution [32,33], this red shift is consistent with the influence of the metal interface and the local environment. It also aligns with the shift observed experimentally for the amide I band of TRP-cage. Besides, D_2O molecules can establish hydrogen-bond interactions with TRP-cage residues similarly to H_2O; however, unlike ordinary water, D_2O may also induce H/D exchange at labile sites of the peptide backbone, altering the hydrogen-bond network and producing characteristic shifts to lower frequencies, particularly in modes containing N—H vibrational contributions [34].

Table 1 summarizes the main published works on protein detection using SEIRA spectroscopy. Some of these studies employ plasmonic nanoantennas for streptavidin detection by exploiting the strong biotin–streptavidin interaction, primarily focusing on achieving high sensitivity in aqueous environments; however, no control over the binding orientation of streptavidin is implemented. Other reported studies establish strong local field enhancement within plasmonic nanogaps, leading to high sensitivity, as demonstrated by the detection of the PSA protein biomarker in artificial blood samples using anti-PSA antibodies capable of binding to different epitopes [35]. Additional studies investigate conformational changes in polypeptides induced by external chemical stimuli [9]. In these cases, a physical gap is introduced between the plasmonic nanoantennas and the polypeptide, as well as between the polypeptide and surrounding molecules, while no control over molecular binding orientation is achieved. Conversely, conformational studies on streptavidin and α-synuclein proteins have implemented a cysteine-residue strategy, similar to that employed in the present work, to control protein binding orientation on biotinylated plasmonic nanoantennas.

Most of the referenced studies use water-based samples, where strong water absorption overlaps with the amide I protein band, or perform characterization on dried samples under non-biological conditions. This work provides an orientational control on target protein binding to the functionalized plasmonic resonators, allowing semi-discrete experimental frequencies vibrations associated to amide I and mixed amide I/II vibrational bands.

4. Conclusions

DFT calculations enabled the assignment of specific vibrational modes contributing to the amide I band of the TRP-cage mini-protein in its 1L2Y conformational state, solvated in water and interacting with a gold cluster that models the local environment of plasmonic resonators. The amide I band was predicted to extend over a wide range of frequencies due to the presence of multiple C═O bonds in varied chemical environments. While the high-frequency C═O stretching vibrations were well decoupled from other modes, the medium- and low-frequency vibrations were accompanied by significant cooperative atomic motion in the studied structure. The design and fabrication of gold plasmonic nanoantennas spectrally tuned to the amide I and amide II vibrational bands of the TRP-cage peptide allowed for the enhancement of the molecule fingerprints in these spectral windows. Furthermore, a biofunctionalization strategy enabled a controlled and reproducible orientation of the TRP-cage peptide on gold nanoantennas, ensuring that the projection of each molecule's dipole moment onto the nanorod's longitudinal axis remained highly consistent. This uniform dipole alignment led to equal vibrational enhancement contributions and enabled the resolution of discrete vibrational modes within the semicontinuous amide I and II bands.

Table 1
Main referenced works on protein detection by SEIRA spectroscopy.

Detected molecule	Plasmonic resonator/functionalization strategy	Medium	Achievement	Controlled molecule orientation	Reference
Streptavidin protein	Gold bypiramids-ATPbiotin	H_2O	LoD ~ 10^{-12} M	No/Four sites for protein binding	[36]
Poly-L-lysine peptide	Gold nanoantennas-11-mercaptoundecanoic acid	D_2O	Conformational changes: α-helix/β-sheet	Partially. Allow peptide folding but it can bind to two thiol sites	[9]
Streptavidin and α-synuclein proteins	Gold nanoantennas-biotinylated PEG-alkane thiol, cysteine-maleimide chemistry through cysteine residue	H_2O/air	Conformational changes: random coil/cross β sheet	Yes	[12]
Streptavidin protein	Gold nanoantennas-biotinylated thiols	H_2O	LoD ~ 100 pg/mL.Study of secondary structure up to 100 pg/mL	No. Four sites for protein binding	[10]
Ig G protein	Gold nanoantennas-biotinylated-PEG-thiol, streptavidin and biotinylated anti-Ig G antibodies	H_2O	LoD ~ 175 ng/cm^2	No	[30]
Streptavidin protein	Gold nanoantennas perpendicularly oriented and HPDP biotin	Air	–	Partially. Orientation deduced from Fano resonance shape	[37]
PSA protein	Gold-Al_2O_3-gold nanogaps, 11-mercaptoundecanoic acid, EDC/NHS	Biological doped samples	LoD ~ 0.15 pM	No	[35]
TRP-cage protein	Gold nanoantennas, SAMs (11-mercapto-1-undecanol and 1,11-undecanedithiol) and cysteine residue	D_2O	amide I and amide II Vibrational bands identification	Yes	This work

This strategy represents a promising route for studying and detecting conformational changes in proteins. Immobilizing the protein in a controlled manner—with precise intermolecular spacing and a small gap introduced between the protein and gold nanoantennas—reduces steric hindrance and facilitates the free vibration of the protein. This setup allows the protein to undergo structural changes in response to external stimuli. For instance, the introduction of a chemical buffer or an increase in temperature could induce protein denaturation, leading to changes in its vibrational fingerprint. However, such analyses must be conducted carefully, as both temperature and chemical conditions can shift the plasmonic resonances of the nanoantennas, thereby altering the coupling between the molecular vibrational modes and the broader plasmonic response.

The computational framework presented here for the TRP-cage molecule provides a highly scalable roadmap for studying larger, more complex proteins. High efficiency is maintained by combining an implicit solvent model [21] with a partial Hessian matrix approach, which restricts the calculation of force constants strictly to the active degrees of freedom at the biomolecule–substrate interface. For significantly larger macromolecular complexes, the numerical effort of standard DFT, which scales cubically with the total atom count, becomes the limiting factor. This limitation can be bypassed by using linear-scaling methods [38], semi-empirical approaches, or machine-learning potentials [39], which drastically accelerate the evaluation of interatomic forces. In addition to this, the biofunctionalization strategy we have implemented produces a single orientation, restricting the degrees of freedom and facilitating the computational simulations, which is particularly convenient for larger systems.

Extending this type of approach to other proteins could enable the development of an experimental and theoretical library of distinct natural vibrational fingerprints corresponding to different conformers. Such a library would improve the ability to identify specific proteins, their conformational states and transitions within complex molecular environments. In this context, the recognition of distinctive vibrational patterns should be complemented by data-driven approaches based on machine learning, including unsupervised methods such as principal component analysis (PCA) and hierarchical clustering analysis (HCA), as well as supervised techniques like support vector machines (SVMs). Additionally, the use of high-brightness broadband infrared lasers sources could facilitate the identification of target discrete vibrational modes for ultrasensitive in-vitro diagnosis down to the single protein level.

Declaration of competing interest

The authors declare that they have no known competing financial interests or personal relationships that could have appeared to influence the work reported in this paper.

Acknowledgement

This work has been partially funded by the Guipuzkoa Quantum program's 2022 under the research project Quantum SEIRA (2022-QUAN-000034-01) and by the Basque Government under the research project ELKARTEK KK-2025/00058. S.M., A.V., and M.Z.H. acknowledge the funding support provided to the research project QSWEAT (2025-QUAN-000010-01), funded by the 2025 Gipuzkoa Quantum Program.

I.V.L. and F.M. acknowledge computer resources at MareNostrum and the technical support provided by Barcelona Supercomputing Center (RES grant no. FI-2025-2-0068).

G.O.Q. acknowledges support by Ikerbasque, the Basque Foundation for Science.

Appendix A. Supplementary data

Supplementary data to this article can be found online at https://doi.org/10.1016/j.mne.2026.100373.

Data availability

Data will be made available on request.

References

[1] J. Yi, E.-M. You, R. Hu, D.-Y. Wu, G.-K. Liu, Z.-L. Yang, H. Zhang, Y. Gu, Y.-H. Wang, X. Wang, H. Ma, Y. Yang, J.-Y. Liu, F.R. Fan, C. Zhan, J.-H. Tian, Y. Qiao, H. Wang, S.-H. Luo, Z.-D. Meng, B.-W. Mao, J.-F. Li, B. Ren, J. Aizpurua, V. A. Apkarian, P.N. Bartlett, J. Baumberg, S.E.J. Bell, A.G. Brolo, L.E. Brus, J. Choo, L. Cui, V. Deckert, K.F. Domke, Z.-C. Dong, S. Duan, K. Faulds, R. Frontiera, N. Halas, C. Haynes, T. Itoh, J. Kneipp, K. Kneipp, E.C. Le Ru, Z.-P. Li, X.Y. Ling, J. Lipkowski, L.M. Liz-Marzán, J.-M. Nam, S. Nie, P. Nordlander, Y. Ozaki, R. Panneerselvam, J. Popp, A.E. Russell, S. Schlücker, Y. Tian, L. Tong, H. Xu, Y. Xu, L. Yang, J. Yao, J. Zhang, Y. Zhang, Y. Zhang, B. Zhao, R. Zenobi, G. C. Schatz, D. Graham, Z.-Q. Tian, Surface-enhanced Raman spectroscopy: a half-century historical perspective, Chem. Soc. Rev. 54 (2025) 1453–1551, https://doi.org/10.1039/D4CS00883A.

[2] Y. Yang, J. Seong, M. Choi, J. Park, G. Kim, H. Kim, J. Jeong, C. Jung, J. Kim, G. Jeon, K-il Lee, D.H. Yoon, J. Rho, Light Sci. Appl. 12 (2023) 152, https://doi.org/10.1038/s41377-023-01169-4.

[3] E.S.A. Goerlitzer, M. Zapata-Herrera, E. Ponomareva, D. Feller, A. Garcia-Etxarri, M. Karg, J. Aizpurua, N. Vogel, Molecular induced chirality transfer to plasmonic lattice modes, ACS Photonics 10 (6) (2023) 1821–1831, https://doi.org/10.1021/acsphotonics.3c00174.

[4] U.F.S. Roggero, C.J. Rojas-Bejarano, C.A. Herreño-Fierro, A. Seifert, A. Garcia-Etxarri, H.E. Hernández-Figueroa, M. Zapata-Herrera, Surface lattice resonances for high performance sensing: a study on gold nanoparticle arrays, Opt. Express 33 (14) (2025) 30328, https://doi.org/10.1364/OE.564444.

[5] F. Neubrech, C. Huck, K. Weber, A. Pucci, H. Giessen, Surface-enhanced infrared spectroscopy using resonant nanoantennas, Chem. Rev. 117 (7) (2017), https://doi.org/10.1021/acs.chemrev.6b00743.

[6] A.G. Nikitin, A.V. Kabashin, H. Dallaporta, Plasmonic resonances in diffractive arrays of gold nanoantennas: near and far field effects, Opt. Express 20 (25) (2012) 27941, https://doi.org/10.1364/OE.20.027941.

[7] H.L. Wang, E.M. You, R. Panneerselvan, S.Y. Ding, Z.Q. Tian, Advances of surface-enhanced Raman and IR spectroscopies: from nano/microstructures to macro-optical design, Light Sci. Appl. 10 (2021) 161, https://doi.org/10.1038/s41377-021-00599-2.

[8] S. Merino, A. Villar, R. D-Ahedo, E. Gárate, I. Amenabar, R. Gay, J. Espina, M. Z.-Herrera, R.A. Boto, J. Aizpurua, Acrylamide molecule detection by surface-enhanced infrared absorption spectroscopy using resonant nanoantennas, Spectrochim. Acta A Mol. Biomol. Spectrosc. 345 (2026) 126772, https://doi.org/10.1016/j.saa.2025.126772.

[9] R. Semenyshyn, M. Hentschel, C. Stanglmair, T. Teutsch, C. Tarin, C. Pacholski, H. Giessen, F. Neubrech, In vitro monitoring conformational changes of polypeptide monolayers using infrared plasmonic nanoantennas, NanoLetters 19 (2018) 1, https://doi.org/10.1021/acs.nanolett.8b02372.

[10] A.J. Herpin, A. Tittl, H. Altug, Quantifying the limits of detection of surface-enhanced infrared spectroscopy with grating order-coupled nanogap antennas, ACS Photonics 5 (2018) 10, https://doi.org/10.1021/acsphotonics.8b00847.

[11] G. Ortega, M. Kurnik, P.D. Ducharme, H. Li, N.A. Curras, A. Caceres, K.W. Plaxco, Surface Attachment Enhances the Thermodynamic Stability of Protein L. https://onlinelibrary.wiley.com/doi/abs/10.1002/anie.201812231.

[12] D. Etezadi, J.B. Warner IV, F.S. Ruggeri, G. Dietler, H.A. Lashuel, H. Altug, Nanoplasmonic mid-infrared biosensor for *in vitro* protein secondary structure detection, Light Sci. Appl. 6 (2017) e17029, https://doi.org/10.1038/lsa.2017.29.

[13] https://www.rcsb.org/structure/1L2Y, 2026. Accesed 09.01.26.

[14] J. Neidigh, R.M. Fesinmeyer, N.H. Andersen, Designing a 20-residue protein, Nat. Struct. Mol. Biol. 9 (2002) 425, https://doi.org/10.1038/nsb798.

[15] Simune Atomistics, S.L., ASAP-2025.1 — Atomistic Simulation Advanced Platform. https://www.simuneatomistics.com, 2026. Accesed: 09.01.2026.

[16] F. Marchesin, P. Koval, Y. Pouillon, I. Lebedeva, A. García, M. García-Mota, A. Kimmel, Atomistic Simulation Advanced Platform (ASAP) for materials modelling with ab initio methods, in: Psi-k Conference 2022, Lausanne (Switzerland), 2022 abstract book.

[17] A.H. Larsen, J.J. Mortensen, J. Blomqvist, I.E. Castelli, R. Christensen, M. Dulak, J. Friis, M.N. Groves, B. Hammer, C. Hargus, E.D. Hermes, P.C. Jennings, P. B. Jensen, J. Kermode, J.R. Kitchin, E.L. Kolsbjerg, J. Kubal, K. Kaasbjerg, S. Lysgaard, J.B. Maronsson, T. Maxson, T. Olsen, L. Pastewka, A. Peterson, C. Rostgaard, J. Schotz, O. Schutt, M. Strange, K.S. Thygesen, T. Vegge, L. Vilhelmsen, M. Walter, Z. Zeng, K.W. Jacobsen, The atomic simulation environment – a Phyton library for working with atoms, J. Phys. Condens. Matter 29 (2017) 27, https://doi.org/10.1088/1361-648X/aa680e.

[18] Preview SIESTA Gitlab Branch Featuring the Implicit Solvent. https://gitlab.com/LePython/siesta-forked/-/tree/psolver-5.4, 2026. Accessed: 09.01.2026.

[19] J.M. Soler, E. Artacho, J.D. Gale, A. García, J. Junquera, P. Ordejón, D.S. Portal, The SIESTA method for ab initio order-N materials simulation, J. Phys. Condens. Matter 14 (2002) 11, https://doi.org/10.1088/0953-8984/14/11/302.

[20] A. García, N. Papior, A. Akhtar, E. Artacho, V. Blum, E. Bosoni, P. Brandimarte, M. Brandbyge, J.I. Cerdá, F. Corsetti, R. Cuadrado, V. Dikan, J. Ferrer, J. Gale, P. García-Fernández, V.M. García-Suárez, S. García, G. Huhs, S. Illera, R. Korytár, P. Koval, I. Lebedeva, L. Lin, P. López-Tarifa, S.G. Mayo, S. Mohr, P. Ordejón, A. Postnikov, Y. Pouillon, M. Pruneda, R. Robles, D. Sánchez-Portal, J.M. Soler, R. Ullah, V. Wen-Zhe Yu, J. Junquera, Siesta: recent developments and applications, J. Chem. Phys. 152 (2020) 204108, https://doi.org/10.1063/5.0005077.

[21] G. Fisicaro, L. Genovese, O. Andreussi, S. Mandal, N.N. Nair, N. Marzari, Soft-sphere continuum solvation in electronic-structure calculations, J. Chem. Theory Comput. 13 (2017) 8, https://doi.org/10.1021/acs.jctc.7b00375.

[22] G. Fisicaro, L. Genovese, O. Andreussi, N. Marzari, S. Goedecker, A generalized Poisson and Poisson-Boltzmann solver for electrostatic environments, J. Chem. Phys. 144 (2016) 014103, https://doi.org/10.1063/1.4939125.

[23] J.P. Perdew, K. Burke, M. Ernzerhof, Generalized gradient approximation made simple, Phys. Rev. Lett. 78 (1997) 1396, https://doi.org/10.1103/PhysRevLett.77.3865.

[24] M. Dion, H. Rydberg, E. Schroder, D.C. Langreth, B.I. Lundqvist, Van der Waals density functional for general geometries, Phys. Rev. Lett. 95 (2005) 109902, https://doi.org/10.1103/PhysRevLett.92.246401.

[25] G.R. Pérez, J.M. Soler, Efficient implementation of a Van der Waals density functional: application to double-wall carbon nanotubes, Phys. Rev. Lett. 103 (2009) 096102, https://doi.org/10.1103/PhysRevLett.103.096102.

[26] COMSOL Multiphysics v5.5, AB, Stockholm, Sweden. http://www.comsol.com.

[27] D. Rodrigo, A. Tittl, N. Ait-Bouziad, A. John-Herpin, O. Limaj, C. Kelly, D. Yoo, N. J. Wittenberg, S.H. Oh, H.A. Lashuel, H. Altug, Resolving molecule-specific information in dynamic lipid membrane processes with multi-resonant infrared metasurfaces, Nat. Commun. 9 (2018) 2160, https://doi.org/10.1038/s41467-018-04594-x.

[28] K. Park, Y. Kim, K. Jin Lee, Analysis of deuterated water contents using FTIR bending motion, J. Radioanal. Nucl. Chem. 322 (2019) 487, https://doi.org/10.1007/s10967-019-06734-z.

[29] J.G. Bayly, V.B. Kartha, W.H. Stevens, The absorption spectra of liquid phase H_2O, HDO and D_2O from 0.7 μm to 10 μm, Infrared Phys. 3 (4) (1963), https://doi.org/10.1016/0020-0891(63)90026-5.

[30] R. Adato, H. Altug, In-situ ultra-sensitive infrared absorption spectroscopy of biomolecule interactions in real time with plasmonic nanoantennas, Nat. Commun. 4 (2013) 2154, https://doi.org/10.1038/ncomms3154.

[31] Aarya, T. Thomas, B.R. Sarangi, S.S. Mojumdar, Rapid detection of Ag(I) via size-induced photoluminescence quenching of biocompatible green-emitting, L-tryptophan-scaffolded copper nanoclusters, ACS Omega 8 (2023) 14630–14640, https://doi.org/10.1021/acsomega.3c00462.

[32] Z. Lai, N.K. Preketes, S. Mukamel, J. Wang, Monitoring the folding of TRP-cage peptide by two-dimensional infrared (2DIR) spectroscopy, J. Phys. Chem. B 117 (16) (2013) 4661, https://doi.org/10.1021/jp309122b.

[33] S. Ye, K. Zhong, Y. Huang, G. Zhang, C. Sun, J. Jiang, Artificial intelligence-based amide-II infrared spectroscopy simulation for monitoring protein hydrogen bonding dynamics, J. Am. Chem. Soc. 146 (4) (2024) 2663–2672, https://doi.org/10.1021/jacs.3c12258.

[34] A. Barth, C. Zscherp, What vibrations tell us about proteins, Q. Rev. Biophys. 35 (4) (2002) 369–430, https://doi.org/10.1017/s0033583502003815.

[35] X. Li, L. Tang, X. Zhang, C. Song, X. Zhang, J. Nong, A. Frisoli, Y. Li, W. Wei, Ultrasensitive detection of prostate-specific antigen via nanogap metasurface sensor, Chem. Eng. J. 533 (2026) 174751, https://doi.org/10.1016/j.cej.2026.174751.

[36] A. Campu, F. Lerouge, D. Maniu, K. Magyari, M. Focsan, Ultrasensitive SEIRA detection using gold nanobipyramids: toward efficient multimodal immunosensor, J. Mol. Struct. 1246 (2021) 131160, https://doi.org/10.1016/j.molstruc.2021.131160.

[37] K.M. Alici, Hybridization of Fano and vibrational resonances in surface-enhanced infrared absorption spectroscopy of streptavidin monolayers on metamaterial substrates, IEEE Trans. Nanotechnol. 13 (2) (2014) 216, https://doi.org/10.1109/TNANO.2013.2296896.

[38] I.V. Lebedeva, A. García, E. Artacho, P. Ordejón, Modular implementation of the linear- and cubic-scaling orbital minimization methods in electronic structure codes using atomic orbitals, R. Soc. Open Sci. 10 (2023) 230063, https://doi.org/10.1098/rsos.230063.

[39] P. Friederich, F. Häse, J. Proppe, A. Aspuru-Guzikl, Machine-learned potentials for next-generation matter simulations, Nat. Mater. 20 (2021) 750–761, https://doi.org/10.1038/s41563-020-0777-6.